ADVANCED FUNCTIONAL MATERIALS
www.afm-journal.de

Giant Thermomechanical Bandgap Modulation in Quasi-2D Tellurium

Naveed Hussain, Shehzad Ahmed, Hüseyin U. Tepe, Kaleem Ullah, Khurram Shehzad, Hui Wu,* and Maxim R. Shcherbakov**

Lattice deformation via substrate-driven mechanical straining of 2D materials can profoundly modulate their bandgap by altering the electronic band structure. However, such bandgap modulation is typically short-lived and weak due to substrate slippage, which restores lattice symmetry and limits strain transfer. Here, it is shown that a non-volatile thermomechanical strain induced during hot-press synthesis results in giant modulation of the inherent bandgap in quasi-2D tellurium nanoflakes (TeNFs). By leveraging the thermal expansion coefficient (TEC) mismatch and maintaining a pressure-enforced non-slip condition between TeNFs and the substrate, a non-volatile and anisotropic compressive strain is attained with $\epsilon = -4.01\%$ along zigzag lattice orientation and average biaxial strain of −3.46%. This results in a massive permanent bandgap modulation of 2.3 eV at a rate S (ΔE_g) of up to 815 meV/% (TeNF/ITO), exceeding the highest reported values by 200%. Furthermore, TeNFs display long-term strain retention and exhibit robust band-to-band blue photoemission featuring an intrinsic quantum efficiency of 80%. The results show that non-volatile thermomechanical straining is an efficient substrate-based bandgap modulation technique scalable to other 2D semiconductors and van der Waals materials for on-demand nano-optoelectronic properties.

1. Introduction

Introducing lattice disorder and symmetry breaking by mechanical straining drastically influences the electronic configuration of 2D semiconductors, which results in bandgap modulation, and hence remains highly attractive for custom-designed optoelectronic and photonic devices operating at broad spectral ranges.[1] Notable approaches for inducing lattice strain in 2D materials include epitaxial growth,[2] mechanical bending,[3–7] chemical doping,[8,9] 2D van der Waals (vdW) stacking,[10,11] alloying,[12,13] applying high-pressure (≲100 GPa),[14,15] integration with nanostructured substrates,[16] and wrinkling architectures.[17] Most of these approaches, however, induce volatile strain, resulting in transient bandgap modulation ΔE_g, and are thus incompatible with optoelectronic device fabrication. Non-volatile lattice straining techniques, on the other hand, suffer from modest strain induction of $\epsilon < 0.5\%$. The highest modulation rate $S = \Delta E_g/\epsilon$, which characterizes the efficacy of a straining technique, has been reported to be ≈300 meV/%.[3] This restricts bandgap modulation to a narrow range of a few hundred meV's, which is insufficient to cover broad spectral bandwidths.[18] Although a non-volatile compressive strain of −2.4% has been observed in millimeter-thick epitaxial perovskite films,[19] achieving substantial non-volatile lattice strain in

N. Hussain, M. R. Shcherbakov
Department of Electrical Engineering and Computer Science
University of California Irvine
Irvine, CA 92697, USA
E-mail: naveedh1@uci.edu; maxim.shcherbakov@uci.edu

N. Hussain, H. Wu
State Key Laboratory of New Ceramics and Fine Processing
School of Materials Science and Engineering
Tsinghua University
Beijing 100084, P. R. China
E-mail: huiwu@mail.tsinghua.edu

The ORCID identification number(s) for the author(s) of this article can be found under https://doi.org/10.1002/adfm.202407812

DOI: 10.1002/adfm.202407812

S. Ahmed
College of Physics and Optoelectronic Engineering
Shenzhen University
Guangdong 518060, P. R China

H. U. Tepe, K. Shehzad
Micro and Nano-Technology Program
School of Natural and Applied Sciences
Middle East Technical University
Ankara 06800, Turkey

K. Ullah
Department of Electrical and Computer Engineering
University of Delaware
Newark, DE 19711, USA

K. Shehzad
Institute of Physics
Silesian University of Technology
Konarskiego 22B, Gliwice 44-100, Poland

ultrathin 2D materials that enables tremendously wide bandgap modulation remains a critical challenge.

Group VI tellurium (Te) is a versatile vdW metalloid that exhibits intriguing properties and has sparked interest in its potential as a promising 2D material due to its ability to stabilize in a few-layer configuration,[20] enabling its applications in mid-IR optoelectronics.[21–23] Nevertheless, its narrow direct band gap of ≈0.35 eV in the bulk form has severely hampered its applications in visible and near-infrared optoelectronics.[24] Theoretically, 2D Te has been predicted to undergo a dramatic bandgap transition (0.35–1.92 eV)[25] via confinement effect[26,27] and mechanical straining,[28] making it promising for visible-NIR optoelectronics. Furthermore, it has been argued that a compressive biaxial stain in 2D Te would enable significant bandgap modulation and robust absorption in ultraviolet-blue region. The practicality of these predictions require non-volatile strain induction in Te, causing a permanent wide bandgap modulation. Current methods that rely solely on mechanical straining have proven ineffective. To this end, thermomechanical straining, which exploits thermal expansion coefficient (TEC) mismatch between a 2D material and the growth substrate can induce a large non-volatile strain. However, weak interfacial adhesion leverages relative slippage during thermal expansion and relaxation, which intrinsically limits TEC strain transfer to 0.2%.[29,30]

Here, we show that the TEC mismatching can be effectively modified by combining it with a large uniaxial (out-of-plane) pressure using a "hot-pressing strategy" that maintains a non-slip condition throughout by boosting interfacial adhesion to increase maximum strain transfer by an order of magnitude. We demonstrate synthesis of quasi-2D Te nanoflakes (TeNFs) by directly hot-pressing agglomerates of tellurium microparticles (TeMPs), and obtained massive bandgap modulation from 0.35 to 2.65 ± 0.1 eV. Such modulation is achieved by non-volatile compressive strain of −4.01%, incorporated in TeNFs during the synthesis.[31,32] The induction of substrate-induced non-volatile strain in TeNFs synthesized on c-sapphire (Al_2O_3), indium tin oxide (ITO) glass, and silicon (Si) substrates was validated by micro-Raman and high-resolution transmission electron microscope (HRTEM) investigations. TeNFs synthesized on sapphire (TeNFs/sapph.) demonstrated the largest strain-tuned bandgap modulation of 2.3 eV and bright blue photoemission, as measured by UV–vis absorption and continuous-wave (C.W.) photoluminescence (PL) emission spectroscopy. Lifetime PL measurements performed on TeNFs reveal a long radiative lifetime of 2.2 ns and high intrinsic quantum efficiency (IQE) of 80%. Computational studies confirm the bandgap widening with biaxial compressive strain, which inhibits van-Hove singularities and promotes radiative recombination. This work provides an insight into thermomechanically induced band gap modulation and broadens the scope of 2D materials and vdW metalloids, transforming the landscape of optoelectronic nanodevices, including LEDs and photodetectors.

2. Thermomechanical Synthesis of Strain-Engineered Tellurium Nanoflakes

Figure 1a shows a typical hot-pressing technique in which agglomerates of TeMPs are molded into quasi-2D flakes by mechanical squashing at a high temperature (350 °C). Te agglomerates were subjected to ≈1 GPa of out-of-plane uniaxial pressure, which limited their thermal expansion to the x-y plane while maintaining non-slip conditions. A thorough synthesis mechanism is described in Text S1 (Supporting Information). A field emission electron microscopy (FESEM) image of a typical quasi-2D trapezoidal Te flake is shown in Figure 1b. Because of its 1D preferred growth along its chiral-chain lattice, which spirals along the [0001] direction, 2D Te preferentially adopts a trapezoid shape, making it easier to distinguish between the *a* (zigzag) and c (armchair) axes.[20] Figure 1c shows an atomic force microscopy (AFM) image of a 7 nm thick TeNF on c-sapphire. The optical microscope image of the same TeNF is displayed in the upper-left inset. We used both pressure and heat to achieve a non-volatile biaxial compressive strain in the crystal lattice of TeNFs. During the transformation from MPs to NFs, the out-of-plane (z-axis) uniaxial pressure maintained the non-slip condition between the TeNFs and the bottom substrate by reinforcing the adhesion. The key feature of our strain induction approach lies in the mismatch in the TEC between the TeNFs and the identical top and bottom substrates during both expansion and contraction processes to enable substrate-induced biaxial lattice shrinkage, resulting in biaxial compressive strain. We employed a variety of substrates, including c-sapphire, ITO, and silicon, to achieve control over the induced compressive strain in TeNFs. However, in the main text of this paper, we mostly focus on the results of TeNFs fabricated on sapphire (TeNFs/Sapph.), as they have been shown to demonstrate the optimal strain transfer. X-ray diffraction (XRD) patterns (shown in Figure S1, Supporting Information) of bulk and as-prepared TeNFs suggest trigonal tellurium with typical hexagonal crystal and P3121 space group. The crystal structure of TeNFs is primarily oriented along (100), unlike bulk which is has its primary orientation along (111). This implies that as-prepared TeNFs are single crystalline in nature, which is in agreement with our prior findings on hot-pressed germanium nanoflakes.[33] The (100) peak for TeNFs shows a distinct shift of $\Delta\theta = 0.5°$ (inset). The shift likely originates from lattice elongation (tensile strain) along the basal plane and serves to preserve the volume of the hexagonal unit cell in response to the biaxial compressive strain induced by the TEC mismatch. The optical microscopy, FESEM, and AFM images of a TeNF fabricated on ITO substrate have been shown in Figure S2a–c (Supporting Information). The energy-dispersive X-ray spectroscopy spectra acquired from an ultrathin TeNF/ITO are shown in Figure S2d,e (Supporting Information), revealing high purity of as-prepared TeNFs. The importance of high pressure in the fabrication of ultrathin TeNFs is symbolized by a crack propagating on ITO (Figure S2e, Supporting Information). However, with strong interfacial adhesion, as seen in our instance, the visible strain release remains heavily concentrated within the cracks,[34] while regions further away remain unaffected and bear a significant amount of strain. According to AFM data, the thickness distribution histogram of 100 thinnest TeNFs on c-sapphire showed a significant percentage (60–65%) of flakes in the 10–30 nm thickness range. (Figure S5c, Supporting Information).

The TEC mismatch between the substrate and TeNFs can induce strain gradient along Te flakes. Thus, we performed COMSOL Multiphysics simulations to spatially map strain during the thermal relaxation. (Figure 1d). The strain gradient at the TeNFs/sapph. interface was introduced during relative thermal contraction and displayed from left to right. The top row shows

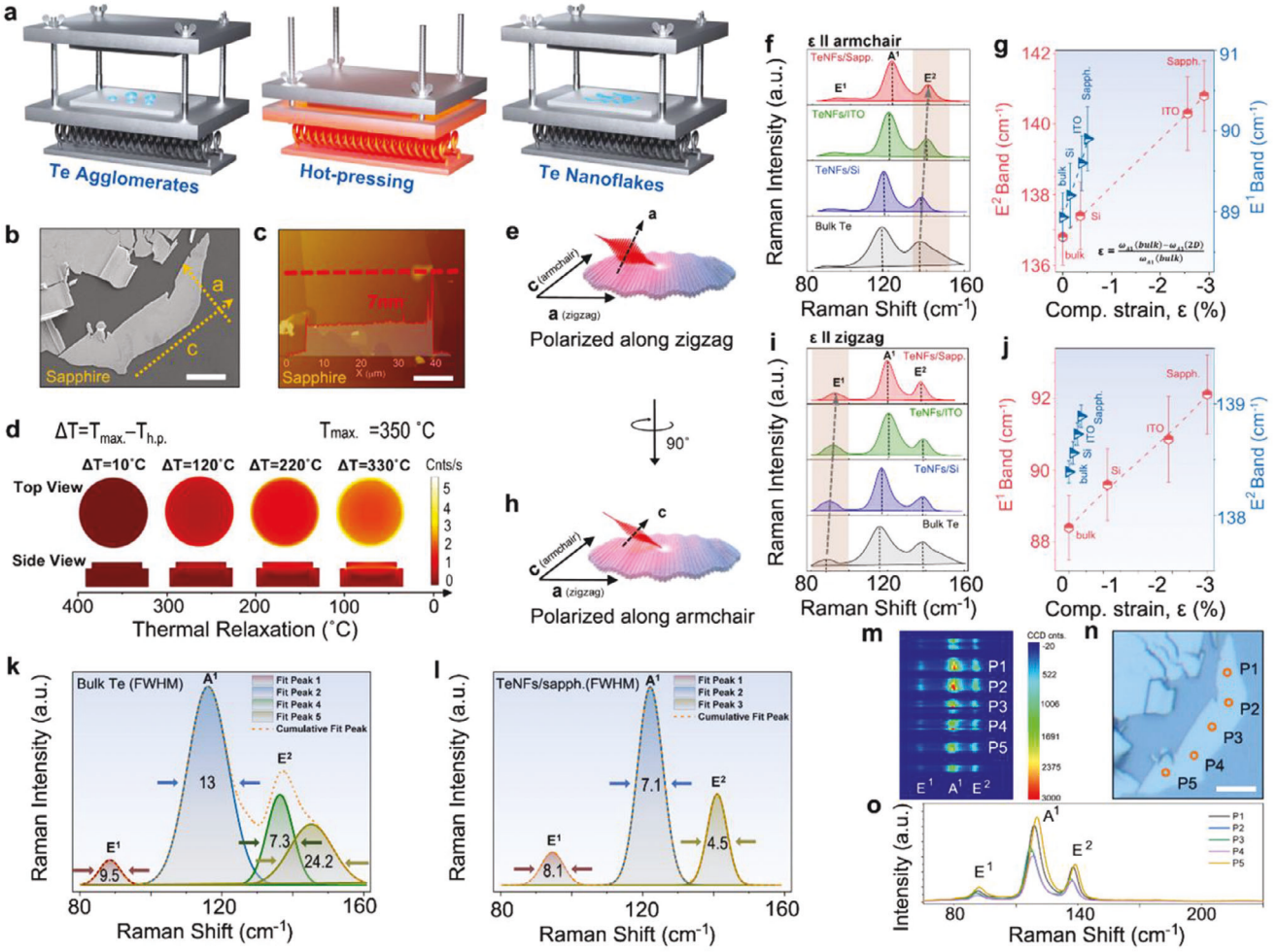

Figure 1. Hot-pressing strategy and μ-Raman spectroscopy characterizations of TeNFs. a) A schematic diagram of the hot-pressing method that mechanically squashes TeMP agglomerates to mold them into ultrathin TeNFs. b) FESEM image of a trapezoid-shaped TeNF lying on c-sapphire, with its zigzag (*a*) and armchair (*c*) axes. c) AFM image of the TeNF/sapphire with the thickness profile of 7 nm. d) COMSOL Multiphysics simulation results show the theoretical calculation of compressive strain and its gradient at the sapphire-TeNF interface during the thermal relaxation process in hot-pressing. e) Multilayer Te flake exposed to 532 nm laser polarized along zigzag (a-axis). f) Comparative Raman spectra of TeNFs/sapph., TeNFs/ITO, TeNFs/Si, and bulk Te. g) blue shift in E^1 and E^2 modes showing compressive strain in response to polarized excitation laser along the zigzag (a-axis), estimating strain along the armchair (c-) axis. h) Multilayer Te flake rotated 90 along z to expose laser polarization along the armchair (c-axis). Te multilayer was exposed to 532 nm laser polarized along armchair (c-axis). i) Comparative Raman spectra of TeNFs/sapph., TeNFs/ITO, TeNFs/Si, and bulk Te. j) blue shift in combined E^1 and E^2 modes showing compressive strain in response to polarized excitation laser along the zigzag (a-axis), revealing strain along the zig-zag (a-) axis. k,l) deconvoluted μ-Raman spectrum obtained from bulk Te and TeNFs/sapph. samples. Peak fitting was performed using Gaussian fitting to estimate the FWHM (Γ) of each vibrational band, which is numerically presented with the corresponding peaks. m) Raman map of an individual TeNF/sapph. and its intensity profile confirming the presence of E^1, A^1, and E^2 phonon modes. n) An optical microscopy image of a Te flake used to acquire Raman spectra along five points P1-P5. o) Combined Raman spectra from points P1–P5, showing strain localization. The scale bars in Figure 1b,c,n are 10 μm each.

the strain gradient from above, while the bottom row shows its cross-sectional view at TeNFs-sapphire interface. When the hot press reaches 350 °C, the interfacial compressive strain is at its minimum because of their maximum thermal expansion state, that is, $T_{max.} - T_{h.p.} = 10$ °C. Here, $T_{max.}$ presents the maximum temperature achieved by the hot-press (350 °C) for TeNFs syntheses, while $T_{h.p.}$ is the variable temperature of the hot-press at different stages of thermal relaxation. The TEC mismatch causes c-sapphire and TeNF to contract at different rates during the thermal relaxation till achieving room temperature ($T_{max.} - T_{h.p.} = 330$ °C), resulting in strain gradient that propagates from the flake edges to the core.[35] We calculated the relaxation constant: $R = (\omega_{\max.strained} - \omega_{2D\ Te})/(\omega_{\max.strained} - \omega_{bulk\ Te})$, where $\omega_{\max.strained}$, $\omega_{bulk\ Te}$, and $\omega_{2D\ Te}$ are the peak shifts (in cm^{-1}) in E^1 and E^2 modes of maximum strained TeNF, bulk Te (relaxed) crystal and that of the TeNF with specific thickness, respectively. It was revealed (Text S4 and Figure S3a–c, Supporting Information) that R is zero at a thickness of 12 nm and unity at a thickness of 60 nm when dislocations occur, plastically relaxing the strain nearby.

For experimental quantification of biaxial compressive strain and to probe phonon vibrational modes in TeNFs, we performed

detailed micro (μ-) Raman characterization on TeNFs/sapph., TeNFs/ITO, TeNFs/Si, and bulk Te sample. The anisotropic structure of Te obligated polarized μ-Raman spectroscopy to probe the structural fingerprints along the a (zigzag) and c (armchair) axes using a linearly polarized 532 nm laser. The axes of TeNFs were easily identified for anisotropic μ-Raman studies due to their characteristic trapezoid shape. The bulk Te Raman spectrum consists of three active phonon modes E^1, A^1, and E^2, located at 89.9, 116.8, and 137.4 cm^{-1}, respectively,[36,37] revealing the trigonal phase tellurium (*t*-Te).[38] The most prominent principal A^1 mode is assigned to lattice vibrations parallel to the basal planes and, therefore, does not contribute to in-plane strain. E^1 and E^2 are degenerate phonon modes primarily attributed to bond-bending caused by the rotation along zigzag and asymmetric band-stretching along the armchair, respectively.[39] Notably, E^1 mode is insensitive to laser polarized along zigzag, and E^2 mode is unaffected by laser polarized along armchair. Therefore, shifts in E^1 and E^2 modes thus yield strain along the zigzag and armchair axes, respectively. Figure 1e shows a hot-pressed Te flake exposed to 532 nm laser polarized along zigzag (a-axis), which probes the lattice strain along the 1D chain direction, that is, armchair.[40] Figure 1f compares the μ-Raman spectra of unstrained bulk Te (black curve) and strained TeNFs on Si (blue curve), ITO (green curve), and sapphire (red curve) substrates. Although no indication of a thermomechanically-induced phase transition was observed, a significant blue shift in E^2 mode confirms a compressive strain along the armchair direction.[41] For samples fabricated on sapphire, ITO, Si, and the bulk Te, the estimated blueshift in both the degenerate (E^1 and E^2) modes (Figure 1g) have been plotted against the estimated compressive strain. The amount of strain and its type is estimated by using $\varepsilon(\%) = [\omega_{A1}(\text{bulk}) - \omega_{A1}(2D)]/\omega_{A1}(\text{bulk}) \times 100\%$, where ω_{A1}(bulk) and ω_{A1}(2D) are the peak values of E^2 phonon modes corresponding to bulk Te and TeNFs, respectively. The significant blue shift in E^2 mode confirmed compressive strain along the armchair direction in all samples, while E^1 mode had a negligible blueshift (blue triangles in Figure 1g) as it insensitive to the laser polarized along the zigzag. We rotated the sample clockwise by 90° to polarize the laser along the armchair direction to measure strain along the zigzag (Figure 1h). The μ-Raman spectra of TeNFs/sapph., TeNFs/ITO, TeNFs/Si, and bulk Te samples were acquired again. All the samples revealed a prominent blue shift in E^1 phone mode, while a negligible blue shift in E^2 mode was observed (Figure 1i). Figure 1j presents the blue shift and the corresponding compressive strain in E^1 and E^2 modes. Due to the inability of the setup to probe the strain along the armchair, only a small amount of compressive strain was detected in comparison to a significant strain along the zigzag. The optimal compressive strain along the zigzag and armchair orientation for TeNFs/sapph. was estimated to be $-4.01 \pm 0.45\%$ and $-2.92 \pm 0.5\%$, respectively. Meanwhile, for TeNFs/ITO samples, the strain along the zigzag and armchair was estimated to be $-2.89 \pm 0.4\%$ and $-2.5 \pm 0.35\%$, respectively; see Table S1 (Supporting Information). We deconvoluted the μ-Raman spectra of both bulk Te and TeNFs/sapph. and the peaks were fitted using the Gaussian function to estimate the full width at half-maximum (FWHM, Γ) of each vibrational mode (Figure 1k,l). All vibrational modes of TeNFs on sapphire exhibited markedly narrower linewidths compared to bulk Te, indicating enhanced crystallinity and decreased native defect density attributed to the thermal annealing during hot-pressing.[42] For amorphous tellurium, a broad peak has been reported ≈170 cm^{-1}, while additional vibrational modes appear at higher frequencies, in the spectral range 350–800 cm^{-1} for tellurium oxide species; TeO_x, as reported elsewhere.[43] Another report suggests the A1 mode related to TeO is located ≈128 cm^{-1}, which is 6 cm^{-1} higher than the maximum observed Raman shift (122 cm^{-1}) in this work.[44] Figure S4 (Supporting Information) shows long range spectra of TeNFs/Si shows no additional peaks ≈170, 450 or 650 cm^{-1}. Instead, a minor background peak associated with silicon has been observed at 520 cm^{-1}. It concludes that there was no evidence found of amorphous or oxide formation. To study the homogeneity of compressive strain in TeNFs/sapph. samples we performed Raman mapping of the phonon modes as shown in Figure 1m. The bright spots represent the phonon modes at points labeled as P1–P5, while Figure 1n shows the optical microscopy image of the flake showing point distribution P1–P5, where the scale bar is 5 μm. The μ-Raman spectra recorded from points P1–P5 (shown in Figure 1n) are displayed in Figure 1o, indicating the strong spatial localization of compressive strain in TeNFs. Thermomechanical staining causes an intrinsic strain localization in TeNF due to the TEC mismatch.

3. Direct Observation of the Post-Treatment Strain

We employed HRTEM as a direct approach to visualize compressive strain induction in TeNFs. Tellurium crystallizes to form a chain-like hexagonal lattice with an infinite helical rotation at 120° along the longitudinal [0001] armchair (*c-axis*) that covalently connects these atoms.[23] The weak vdW force along the zigzag direction binds all turns to hexagonal bundles in the radial direction. **Figure 2**a,d show transmission electron microscopy (TEM) and HRTEM images of a thick flake reminiscent of unstrained bulk Te, providing the reference lattice constants of 2.3 and 5.9 Å along the armchair and zigzag axes, respectively, attributed to trigonal tellurium (t-Te).[17,26] Figure 2b,c,e,f show low- and high-magnification HRTEM images of ultrathin of TeNFs/sapph. and TeNFs/ITO samples, respectively. Figure 2b presents the low-resolution HRTEM image, while the inset shows the TEM image of the TeNF. Figure 2c shows a magnified HRTEM image collected from the area highlighted by the red box in Figure 2b. A characteristic lattice compression along both axes was observed, where lattice constants shrank by ≈0.22 ± 1 Å (5.9–5.68 ± 1Å) along the zigzag and 0.1 ± 1 Å (2.3–2.20 ± 1Å) along the armchair axes. Figure 2e presents the TEM image (inset) and low-resolution HRTEM image of TeNF/ITO. The HRTEM image (Figure 2f) shows the lattice compression of ≈0.2 ± 1 Å (5.9–5.7 ± 1 Å) along the zigzag and 0.08 ± 1 Å (2.3–2.22 ± 1 Å) along the armchair axes. Due to the instrument's resolution limit of 0.1 nm, the strain values derived from HRTEM analyses somewhat surpassed those calculated by Raman analysis. As a result, the HRTEM results have a marginally lower level of accuracy. The inset in Figure 2c shows nanocompression in TeNFs/sapph. The SAED patterns collected from both samples also confirmed the angular compression between the axes, revealing the highly crystalline nature of TeNFs fabricated on both substrates. The diffraction points along the zigzag are visible,

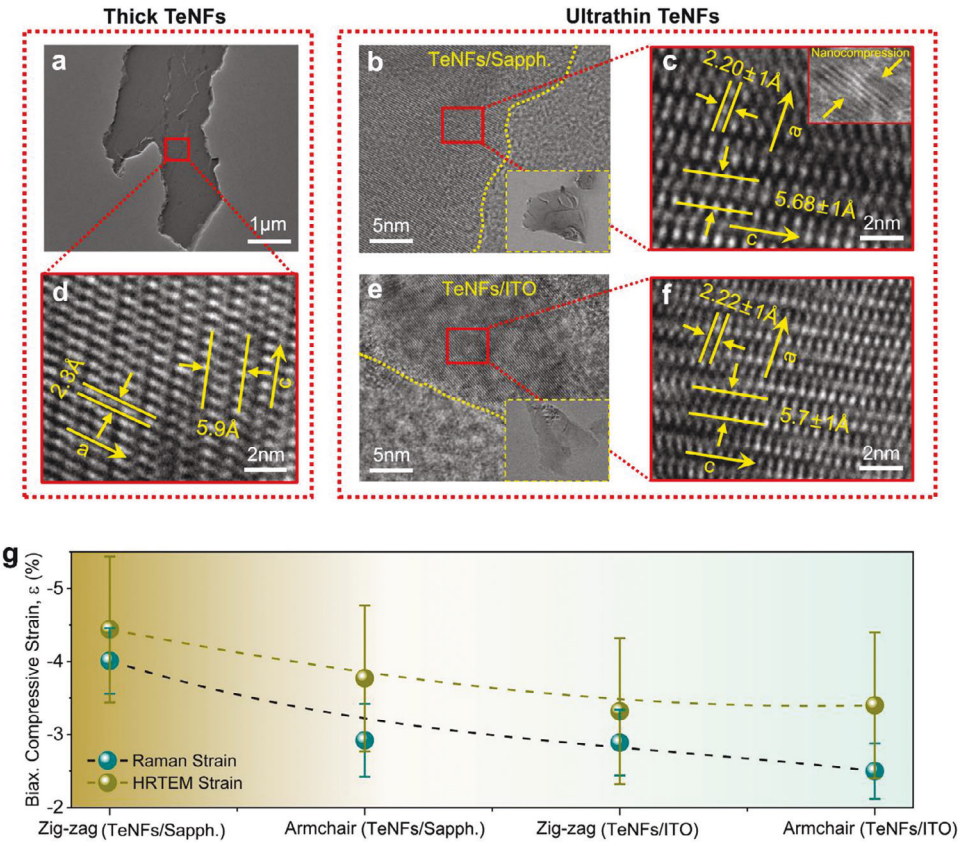

Figure 2. Direct strain estimation of treated Te with comprehensive electron microscopy. a) TEM image of a thick TeNF reminiscent of bulk Te. b) Low magnification HRTEM image acquired from the TEM image shown in the inset for TeNFs/sapph. sample. c) HRTEM image showing lattice compression along both axes. d) HRTEM image acquired from the area in panel A highlighted with a red rectangle in, shows standard lattice parameters along zigzag and armchair. e) Low magnification HRTEM image acquired from the TEM image shown in the inset for TeNFs/ITO sample. f) HRTEM image showing lattice compression along both axes. g) the comparison between the strain values estimated using micro-Raman spectroscopy (green line), and by electron microscopy (TEM/HRTEM) (light yellow) along both the axes in TeNFs/sapph. and TeNFs/ITO samples. The error bars were acquired by repeating each measurement 5 times. The inset shows evidence of nanostraining in the form of nanoripples in TeNFs.

making it easier to determine the other axis (Figure S5a,b, Supporting Information).

We compared the compressive strain values obtained by two independent approaches in Figure 2g. The green and light-yellow lines with error bars represent the compressive strain in TeNFs obtained using μ-Raman and HRTEM, respectively. The results were in striking agreement with the experimental uncertainties and suggested that the overall strain in TeNF/ITO was quantitatively less than that of TeNF/sapph. The inset shows evidence of nanostraining in TeNF/sapph. in the form of nanowrinkles. The ESD mapping spectrum showing a strong Te signal is presented in Figure S5d (Supporting Information).

The bulk tellurium lattice parameters along the zigzag and armchair axes can be determined at various temperatures between 25 and 350 °C using the following equations: $a_{Te} = a_o + 168.3 \times 10^{-6}\ t - 12.68 \times 10^{-8}\ t^2$ and $c_{Te} = c_o - 14.99 \times 10^{-6}\ t$, respectively.[45] According to these equations, heating Te to 350 °C without maintaining the interfacial non-slip condition (i.e., without uniaxial pressure) would only induce a strain of ≈0.166% and ≈0.25% along armchair (a_c) and the zigzag (c_a), respectively. This indicates that achieving such high strain values in TeNFs necessitates the combination of both uniaxial pressure and heating.

4. Optical Interrogation of Giant Bandgap Modulation and Exciton Dynamics

Strain induction influences TeNFs band structure, which we investigated using steady-state *C.W.* and time-resolved PL, absorbance, and emission spectroscopy characterizations over a single 12 nm thick TeNF with UV to NIR excitation wavelengths. **Figure 3a** illustrates the absorbance (green dashed line) and μ-PL emission spectra (solid blue line) of TeNF and bulk Te (black line) excited by a 325 nm C.W. pump. The narrow bandgap of 0.35 eV prevented bulk Te from showing PL response in the UV-IR region, except for a weak hump at 1.9 eV attributed to native defect states. In contrast, TeNFs exhibited an intense PL emission signal in the blue region of the spectrum, peaking at 2.62 eV, confirming an enormous bandgap (E_g) widening to the blue spectral region. The optical E_g of 2.65 eV was estimated by extrapolating the tangent line of the absorbance measurements using the Tauc-plot, presented as Figure 3b. The results confirmed that the compressive strain caused a significant E_g shift of 2.3 eV. As measured by a fluorescence microscopy imaging technique, the strong blue photoemission in TeNF/sapph. in Figure 3c is compelling evidence of E_g modulation. PL map of the same TeNF is given in

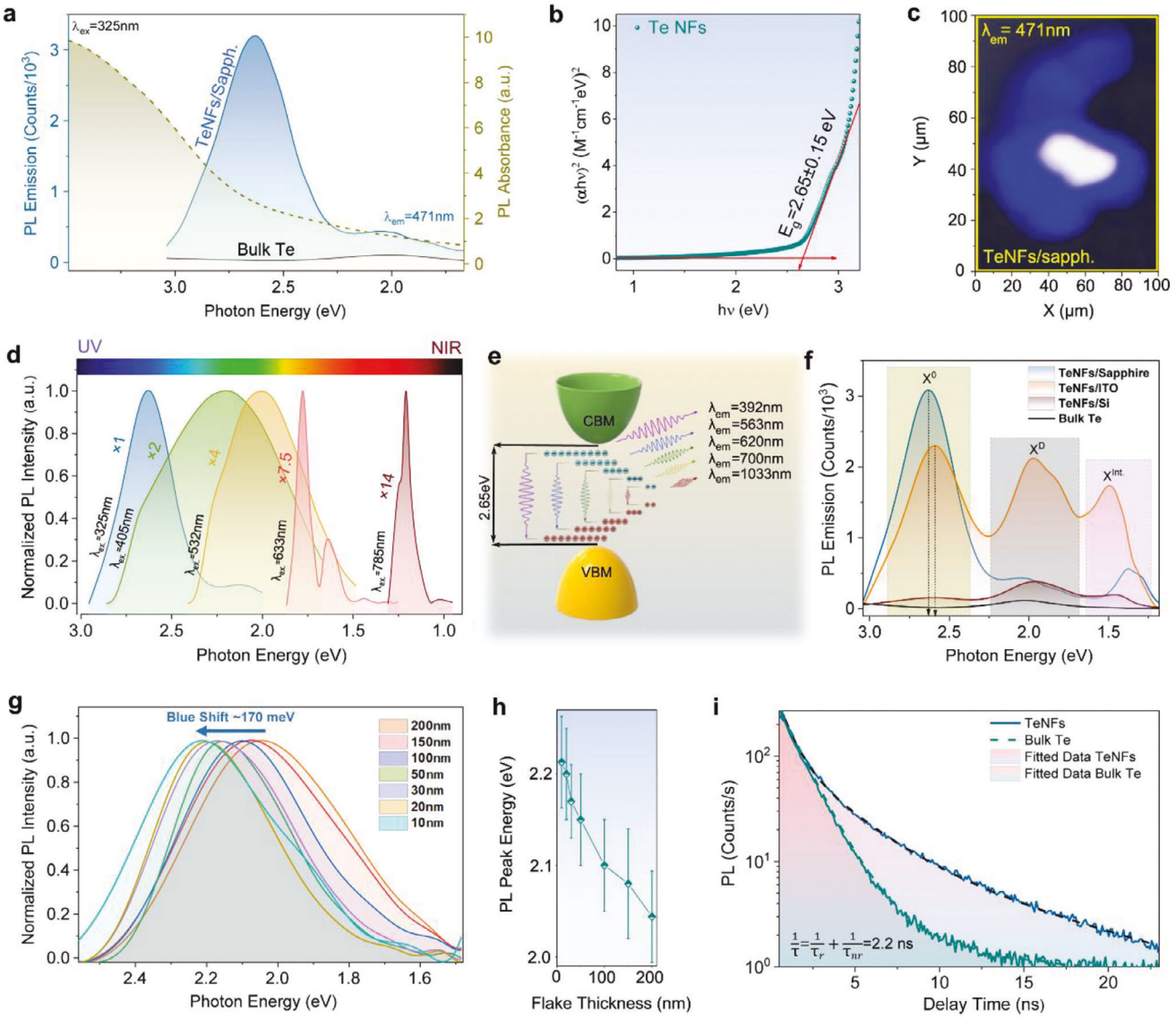

Figure 3. Optical determination of bandgap modulation and exciton dynamics in TeNFs. a) PL absorbance and emission spectra of TeNFs/sapph. acquired at 300 K, using 325 nm laser. b) the Tauc plot for band gap estimation, while another inset is the fluorescence microscopy image of an individual TeNF/sapph. exhibiting strong blue photoemission. c) PL mapping image of a TeNF, excited at 532 nm laser excitation. d) Excitation wavelength-dependent PL emission in TeNFs/sapph. e) Schematic of sub-band transitions with different excitation wavelengths. f) substrate-dependent PL emission responses from TeNFs/sapph., TeNFs/ITO, TeNFs/Si, and bulk Te samples. g) Thickness-dependent PL emission in TeNFs/sapph. h) The variation in PL peak energy with flake thicknesses. i) Lifetime PL emission spectra of TeNFs. The inset shows the comparative TRPL curve of bulk and TeNFs.

Figure S6a,b (Supporting Information), showing spatial PL localization in TeNFs. The deconvolution of the TeNF/sapph. suggested that its spectrum consisted of a triplet state in the visible part of the spectrum (Figure S7a, Supporting Information). The red-highlighted peak X^0 at 2.62 eV corresponds to the band-edge recombination of electron-hole (*e-h*) pairs.[46] The large width of the X^D peak (highlighted in green) at ≈1.78 eV suggests radiative *e-h* recombination due to native defect states. However, the origin of the peak $X^{Int.}$ at 1.3 eV remains unknown. We hypothesize that this may be attributable to either the loosely bound surface oxide species on TeNF surfaces or the emission resulting from the TeNFs/sapph. interfacial states. More investigation is required to provide a plausible explanation for this PL peak's origin. It must be noted that the unstrained tellurium microcrystals have been shown to emit light in the mid-infrared range.[47]

The interband transitions were investigated by exciting TeNFs/sapph. with a range of wavelengths, including 325, 410, 532, 633, and 785 nm. We observed a PL emission peak in response to all excitation sources, indicating the emergence of subband states within the modulated bandgap of TeNFs (Figure 3d). One may argue that the PL emission across the vis-NIR spectral region in response to the aforementioned laser excitations is due to the introduction of subband defect states. However, our Raman studies (see Figure 1k,l) show a significant decrease in

the FWHM of all vibrational modes, signifying a decrease in the native defect density of TeNFs, particularly on sapphire, with no apparent substrate-induced defects. As a result, this rationale is ruled out, establishing that sub-band PL emission is indeed attributed to the opening of the band gap in TeNFs. The PL intensity in response to longer excitation wavelengths reduced significantly, as shown in Figure S7b (Supporting Information). The schematic illustration of interband transitions in TeNFs has been presented in Figure 3e. The substrate-dependent comparative PL emission spectra of TeNFs/sapphire (blue), TeNFs/ITO (orange), TeNFs/Si (wine), and bulk Te (cyan) are shown in Figure 3f. It is evident that the ITO substrate also played a key role in the significant bandgap opening of TeNFs; however, it also had other enhanced and broad peaks that included contributions from native defects and the TeNFs/ITO interfacial states. We performed thickness-dependent PL studies, which revealed a two-orders-of-magnitude monotonic decrease in PL intensity as flake thickness decreased from 200 to 10 nm. (Figure 3g). This could be attributed to the fewer *e-h* pairs available at longer excitation wavelengths, resulting in a lower absorption cross-section. This dependence is well described by the following expression: $I_{PL} = I_{Te}[1–\exp(–a_{Te}h_{flake})]$, where I_{Te} is the PL intensity of the TeNF with h_{flake} = 200 nm.[48] The absorption coefficient a_{Te} = 5000 cm^{-1} was used.[49] We also observed an overall blue-shift of 170 meV in the PL peak energy with decreasing flake thicknesses from 200 to 10 nm, a signature We also observed a 170 meV blue-shift in the PL peak energy as the flake thickness decreased from 200 to 10 nm, a signature of quantum-size effects in strained TeNFs. Figure 3h reveals the variation in PL peak energy with flake thicknesses, while the variation in PL peak intensity with flake thicknesses has been presented in Figure S7c,d (Supporting Information). The PL peak energy trend with the TEC of growth substrates has been presented in Figure S7e (Supporting Information). No contribution to the PL signal from the sapphire substrate was observed, which usually has an intense sharp peak at 1.79 eV (Figure S8, Supporting Information). Comprehensive XPS studies (Text S3 and Figure S9, Supporting Information) showed a pure metallic phase without oxide signatures, ruling out oxidation-induced PL signal. Figure 3i displays time-resolved photoluminescence (PL) traces of bulk Te and TeNFs, collected under ambient conditions using time-correlated single photon counting with an excitation wavelength of 325 nm. The data was fit using a bi-exponential fitting equation to understand the exciton dynamics in TeNFs.[50] In comparison with the PL decay curve of bulk Te (green curve), the decay (blue) curve of TeNFs showed enhanced carrier recombination lifetimes, where the shorter lifetime component (τ_1) increased threefold, from 0.21 to 0.73 ns. Similarly, the longer lifetime component (τ_2) almost doubled from 1.39 to 2.84 ns. This, along with the strong PL from TeNFs, suggests that the bandgap opening has reduced the non-radiative recombination component in TeNF. This conclusion is further corroborated by our Raman studies, which reveal a significant decrease in the native defect density. A lower defect density translates to fewer non-radiative recombination pathways, resulting in enhancement in radiative recombination od excitons. The carrier recombination lifetime (τ) for TeNFs was determined to be 2.22 ns by using the equation: $\tau^{-1} = \tau_{nr}{}^{-1} + \tau_r{}^{-1}$, where τ, τ_r, τ_{nr} are the average, radiative and non-radiative lifetimes, respectively. The avg. carrier recombination lifetime of bulk Te was estimated to be 1.2 ns, which is ≈50% less than that of TeNFs. The internal quantum efficiency, IQE (η) of TeNFs was calculated by using the following equation[51]:

$$IQE_{PL} = \eta = \tau_r^{-1} / \left(\tau_{nr}^{-1} + \tau_r^{-1}\right) = \tau/\tau_r \quad (1)$$

The η of TeNFs was calculated to be 80%, indicating that photogenerated excitons undergo a robust radiative recombination process. Compressive strain induces a splitting between the Van-Hove singularity resonance and the exciton transition energy, resulting in a significant suppression of exciton-exciton annihilation and a promotion enhancement of the radiative recombination process.[52]

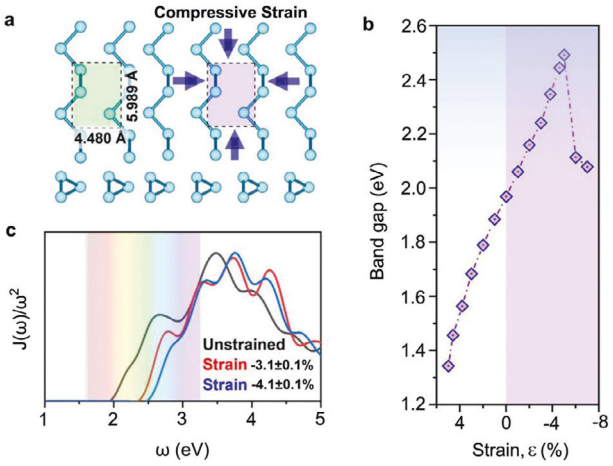

Figure 4. Ab initio simulations of strain-induced bandgap modulation. a) Snapshots of layered Te, top view, and side view, the dashed lines show the primitive unit cell (with lattice vectors a-and b-). b) Hybrid functional HSE06 predicted band gap effects on layered Te as a function of strain. Starting with the relaxed structure, the band gap experiences a transition with both tensile and compressive strain, which agrees with that predicted by the standard DFT. Although DFT underestimates the band gap, its calculated gap-strain variation trend is consistent with HSE06. c) HSE06-based joint density of states ($J(\omega)/\omega^2$) of the relaxed and strained Te layer, respectively.

5. Calculations of Permanent Strain-Induced Band Gap Modulation

Density functional theory (DFT), as implemented by the Vienna ab initio simulation program (VASP), was used to perform electronic and optical calculations.[53] for Te valence orbitals and electrons for pseudoatoms were $5s^2$ and $5p^4$, respectively. As shown in **Figure 4a**, the compressive strain on monolayer Te is applied by varying the cell parameters (a and b, equally). When additional compressive strain is applied, the in-plane xy atomic orbitals overlap significantly, which has a significant effect on the inner energy states and energy shift. As shown in Figure 4b, band gap decreases for tensile-strained monolayer Te and increases for compressively strained monolayer. This matches band gap calculations for strained mono-layer and bi-layer MoS_2.[54,55] A distinct pattern for the band gap shifts is seen when compressive strain in the range of 0–−4.01% is applied. From the density of states (DOS), one can calculate a joint density of states

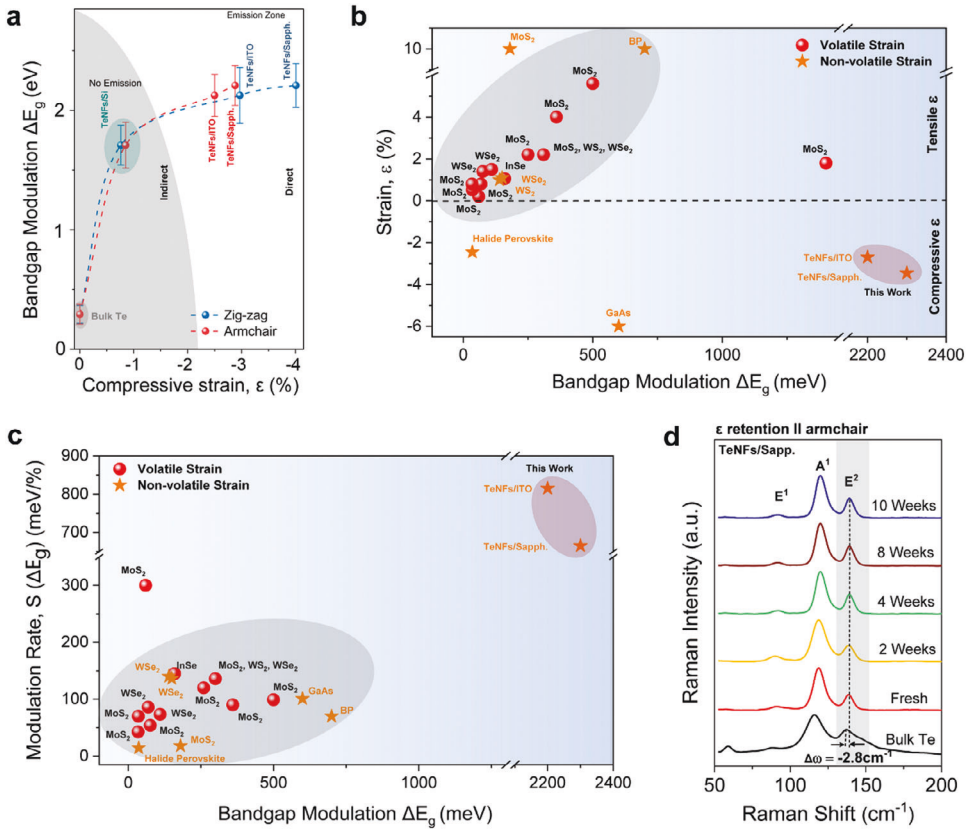

Figure 5. Bandgap modulation, modulation rate, and long-term strain retention in TeNFs. a) the overall bandgap modulation in TeNFs synthesized on Si, ITO, and sapphire substrates in response to the compressive strain. b) Previously reported overall bandgap modulation in 2D materials versus our work. The yellow star and red dots show non-volatile and volatile strain, respectively, while negative and positive strain values are associated with compressive ad tensile strain. c) Modulation rate, S(ΔE_g) in response to bandgap modulation for previously reported works, where yellow stars represent works reporting non-volatile strain induction. d) time-dependent μ-Raman spectra showing long-term strain retention in TeNFs/sapph.

$J(\omega)$ to reveal the origin of the difference in absorption between unstrained and strained phases (neglecting oscillator matrix elements and excitonic effects). The basis of the shift in the absorption of these phases is finally revealed by a detailed analysis of the components of the optical absorption spectra—the joint density of states (Figure 4c). The electron localization function of both the unstrained and strained TeNFs, the corresponding absorption spectrum, and the DOS plot of unstrained (ϵ = 0%), TeNFs/ITO ($\epsilon_{avg.}$ = –2.72%) and TeNFs/sapph. ($\epsilon_{avg.}$ = –3.46%) have been presented in Figure S10a–c (Supporting Information).

6. Discussion

The bandgap modulation in response to the compressive strain introduced along both axes in TeNFs fabricated on various substrates is shown in **Figure** 5a. Even though the strain achieved in TeNFs/Si is ≈–1%, modulating the bandgap by 1.9% is insufficient to trigger the indirect-to-direct bandgap transition, as evidenced by the absence of PL emission. Despite significant bandgap modulation, the shaded gray area corresponds to the region devoid of emission. Nonetheless, strong PL emissions were detected for TeNF/ITO and TeNFs/sapphire, indicating a switchover to the emission zone in modulated bandgap. Due to the weak vdW interaction, it is also evident that the compressive strain is not uniform along both axes for both samples, with the strain along the zigzag axis being greater than that along the armchair axis, attributed to the weak vdW forces.[17] Figure 5b depicts the bandgap modulation (ΔE_g) in response to strain type and its values for previously reported 2D material systems. The red dots represent the engineering of volatile or transient strains in 2D materials, while the yellow stars represent the engineering of non-volatile strains. The induction of compressive and tensile strains is represented by the negative and positive strain values, respectively. The maximum value of non-volatile strain reported in 2D black phosphorus provides an overall ΔE_g of 600 meV, whereas we achieved ΔE_g values of 2.31 eV for TeNF/sapph. and 2.25 eV for TeNF/ITO. The modulation rate S (ΔE_g), defined as the bandgap modulation per percentage strain (meV/%), is a measure of the efficiency of the straining mechanism. Figure 5c provides a comparative summary of the modulation rate reported for various 2D materials to date. The highest S(ΔE) reported to date is 300 meV/%, which was achieved in MoS_2 using a gated piezoelectric substrate, a strategy that cannot be maintained.[3] Through the hot-pressing synthesis of TeNF/ITO and TeNFs/sapphire, we have achieved S(ΔE_g) values of 815 and 665 meV/%, respectively. Raman spectroscopy is a powerful non-destructive technique which can directly probe changes in chemical bonds and oxidation levels by

shifts in these peaks of vibrational modes. We repeated Raman studies on TeNFs/sapphire samples every two weeks for 10 weeks to study their stability and strain retention. After 10 weeks, the E^2 vibrational mode retained its blue shift, and no new oxide-of associated peaks emerged after 10 weeks. This confirms the induction of inherited non-volatile strain with no evidence of considerable oxidation of TeNF. Figure S11 (Supporting Information) shows time-dependent PL studies. After one week of ambient environment exposure, photobleaching caused by surface degradation reduced PL intensity by 31% compared to freshly prepared TeNFs/sapphire samples.[56] The PL intensity remained constant from weeks 2–10, indicating high optical quality and bandgap retention in TeNFs. Future studies on realizing vdW heterostructure of strained tellurium nanoflakes and h-BN are critical to eliminate substrate effects on PL properties, enabling advanced bandgap control for optoelectronics.

7. Conclusion

This work employs hot pressing = to impose a giant bandgap modulation in synthesized quasi-2D elemental Te by introducing a large thermomechanically-induced strain. Hot-pressed TeNFs, sandwiched between c-sapphire, ITO, and Si substrates, undergo a large compressive strain of up to −4.01% due to the reinforced substrate-TeNF adhesion-assisted TEC, resulting in a substantial permanent bandgap modulation from 0.35 to 2.65 eV). The large bandgap modulation rate of 815 meV/% was obtained in TeNF/ITO. DFT calculations confirm the bandgap widening with biaxial compressive strain, which induces suppression of exciton-exciton annihilation, enhanced long-lived radiative carrier recombination and blue photoemission in strained TeNFs. Hence, by manipulating the substrate-induced lattice strain, hot pressing can introduce large bandgap modulation in 2D materials, benefiting cross-disciplinary fields, including on-demand optoelectronics.

8. Experimental Section

Materials: Commercially available TeMPs with the size distribution of 10–50 µm (Sigma–Aldrich, 99.99%) were used without any processing, to prepare an ethanol/TeMPs (50 mL/10 mg) dispersion. Atomically flat (10 × 10 mm^2) c-cut sapphire (Al_2O_3) substrates (KYKY Technology Co. LTD) were ultrasonicated in acetone, ethanol, and distilled water. To obtain moisture-free surfaces of c-sapphire before mass-loading, the substrates were placed in a furnace maintained at 70 °C for 30 min. A commercial hot-press system (AH-4015, 200 V-20A, Japan) was used for thermo-mechanical squashing of TeMPs to fabricate ultrathin TeNFs.

Fabrication of TeNFs: Mass-loading was performed by drop-casting the 20 µL of the homogeneous ethanol/TeMPs dispersion onto the c-cut sapphire substrate by using a micropipette. The loaded substrate was left to dry for 30 min in an argon-filled glove box (MB200MOD) to avoid unnecessary exposure to moisture and dust particles. After the complete evaporation of ethanol, the c-sapphire substrate capped with large agglomerates of TeMPs of different sizes and shapes was taken out of the glove box. It was further covered by another sapphire substrate, thus sandwiching the TeMPs. This sandwiched assembly (sapphire-TeMPs-sapphire) was then placed in the middle of the metal plates of the hot-press machine. During thermo-mechanical squashing, the temperature of the hot press is raised from T_{room} to 350 °C, while the pressure was gradually increased from the atmospheric pressure to 1 GPa. The sapphire-TeMPs-sapphire assembly was hot-pressed for 30 min at 350 °C before allowing thermal relaxation to T_{room}, while maintaining a constant pressure of 1 GPa throughout the relaxation process. Hot-pressing technique molds TeMPs into thin sheets. To achieve this, the temperature needs to be high enough to soften the tellurium (≈60–80% of melting point). For tellurium, 350 °C (77% of its melting point in °C) was chosen. Pressure was then limited by the durability of the sapphire substrate (cracking above 1 GPa). The fabrication of uniform and ultrathin TeNF was optimized by gradually increasing pressure from 0 to 1.0 GPa at a fixed temperature of 350 °C. The results are presented in Figure S12 (Supporting Information). The obtained samples have been studied without any post-fabrication annealing.

Material Characterizations: Morphology of TeNFs was studied by using field emission scanning electron microscopy (FESEM), (MERLIN VP compact, Carl Zeiss, Germany). A multipurpose JEOL-2100 analytical electron microscope with a resolution of 0.1 nm, operated at 200–80 kV, was used to perform the transmission electron microscopy (TEM), high-resolution transmission electron microscopy (HRTEM) and selected area electron diffraction (SAED) measurements. To prepare TEM samples, c-sapphire capped with hot-pressed TeNFs was immersed in ethanol and ultra-sonicated for 30 min to isolate TeNFs from sapphire into the ethanol solution. The ethanol containing SeNFs was dropped onto the carbon-coated Cu grid by a micropipette to perform TEM/HRTEM characterizations. For scanning probe microscopy characterizations, an Asylum Research Cypher AFM (SPM, SHIMADZU Corporation, spm-9600) in tapping mode was employed to investigate surface topography and thicknesses of TeNFs on sapphire and ITO. A Raman spectrometer (LabRAM HR Evolution, HORIBA Jobin Yvon, France) with an objective lens (Nikon Plan Fluor 50 X, N.A. = 0.4) and the laser spot size of ≈2 µm was deployed to acquire Micro-Raman spectra of stained TeNFs lying on a c-sapphire. X-ray photoelectron spectroscopy (XPS, Escalab, 250 Xi, Thermo Fisher Scientific, MA, USA), equipped with an A1Kα radiation source (1487.6 eV), is used to investigate the chemical composition and stoichiometry of TeNFs. The binding energy calibration is performed carefully by using C1s peak (284.8 eV) as a reference value. PL measurements of TeNFs from T_{room} to cryogenic temperatures with variable laser power ranging from 0.2 to 1 mW are performed by using LabRAM HR Evolution, HORIBA Jobin Yvon, France, equipped with a 532 nm Nd: YAG (Nd: $Y_3Al_5O_{12}$) laser, and a CCD detector.

DFT Calculations: First-principles calculations were performed using the projector augmented wave method as implemented in VASP.[57] coupled with generalized gradient approximation (GGA) electron-electron interaction defined as Perdew–Burke–Ernzerhof (PBE) exchange-correlation functional. To prevent interactions between layers brought on by the periodic boundary condition, a vacuum layer with a thickness of ≈25 Å along the z-direction. A plane-wave basis set with a kinetic energy cut-off of 650 eV and PBE projected augmented wave pseudopotential was adopted to expand the wave functions to describe the electron-ion potential, respectively.[58] For structural relaxation, the Monkhorst-Pack method was used to mesh the reciprocal space at 21 × 19 × 1. To get a more precise band gap, the screened hybrid functional approach at the HSE06 level was also used.[59] The weak vdW interaction between the two monolayers was described by the DFT-D2 correction of Grimme.[60] All atoms were relaxed with predicted forces of less than 0.01 eV $Å^{-1}$ and total energies of less than 10^{-6} eV/atom. Optimized mono layer Te unit cell with lattice parameters a = 4.48 Å, b = 4.598 Å, and c = 25 Å were considered.[41,61,62] The lattice parameters were slightly larger while in good agreement with the available experimental results.

Pressure Calculation: The pressure applied during hot-press for mechanically squashing TeMPs to fabricate ultrathin TeNFs is estimated by the following expression:

$$P = \frac{P_0 \times A_0}{a_0} = \frac{\left(55 \times 10^6 Nm^{-2}\right)\left(3.1416 \times \left(24 \times 10^{-3} m\right)^2\right)}{\left(1 \times 10^{-4} m^2\right)}$$
$$= 0.996GPa \cong 1GPa \quad (2)$$

Where P_0 is the applied pressure, A_0 is the area of the cylinder, and a_0 is the area of the substrate.

Supporting Information

Supporting Information is available from the Wiley Online Library or from the author.

Acknowledgements

N.H. and S.A. contributed equally to this work. This material is based upon work supported by the National Science Foundation under Grant no. ECCS-2339271. This study was supported, in part, by the National Key Research and Development Program (2019YFB2203400), the National Basic Research of China (2018YFB0104404), and the National Natural Science Foundation of CHina (12150410313). The authors acknowledge the use of facilities and instrumentation at the UC Irvine Materials Research Institute (IMRI) supported in part by the National Science Foundation Materials Research Science and Engineering Center program through the UC Irvine Center for Complex and Active Materials (DMR-2011967). N.H. initiated the project after consultation with H.W. N.H. synthesized and performed structural optical characterizations of TeNFs. A.S. performed HSE and DFT calculations. H.T. performed COMSOL Multiphysics simulations. N.H., M.S., and K.S. performed the data analysis. N.H. and A.S. wrote the manuscript with contributions from all other authors. N.H. and M.S. supervised the project.

Conflict of Interest

The authors declare no conflict of interest.

Data Availability Statement

The data that support the findings of this study are available from the corresponding author upon reasonable request.

Keywords

bandgap, engineering, hot pressing, non-volatile strain, optoelectronics, tellurium

Received: May 7, 2024
Revised: June 23, 2024
Published online: July 12, 2024

[1] H. Kim, S. Z. Uddin, D.-H. Lien, M. Yeh, N. S. Azar, S. Balendhran, T. Kim, N. Gupta, Y. Rho, C. P. Grigoropoulos, *Nature* **2021**, *596*, 232.
[2] J. A. Del Alamo, *Nature* **2011**, *479*, 317.
[3] Y. Y. Hui, X. Liu, W. Jie, N. Y. Chan, J. Hao, Y.-T. Hsu, L.-J. Li, W. Guo, S. P. Lau, *ACS Nano* **2013**, *7*, 7126.
[4] M. Zeng, J. Liu, L. Zhou, R. G. Mendes, Y. Dong, M.-Y. Zhang, Z.-H. Cui, Z. Cai, Z. Zhang, D. Zhu, *Nat. Mater.* **2020**, *19*, 528.
[5] R. Schmidt, I. Niehues, R. Schneider, M. Drüppel, T. Deilmann, M. Rohlfing, S. M. De Vasconcellos, A. Castellanos-Gomez, R. Bratschitsch, *2D Mater.* **2016**, *3*, 021011.
[6] H. J. Conley, B. Wang, J. I. Ziegler, R. F. Haglund Jr, S. T. Pantelides, K. I. Bolotin, *Nano Lett.* **2013**, *13*, 3626.
[7] C. Zhu, G. Wang, B. Liu, X. Marie, X. Qiao, X. Zhang, X. Wu, H. Fan, P. Tan, T. Amand, *Phys. Rev. B* **2013**, *88*, 121301.
[8] D. Wei, Y. Liu, Y. Wang, H. Zhang, L. Huang, G. J. N. Yu, *Nano Lett.* **2009**, *9*, 1752.
[9] F. Yavari, C. Kritzinger, C. Gaire, L. Song, H. Gulapalli, T. Borca-Tasciuc, P. M. Ajayan, N. J. Koratkar, *Small* **2010**, *6*, 2535.
[10] N. Kharche, S. K. J. N. l. Nayak, *Nano Lett.* **2011**, *11*, 5274.
[11] K. Kośmider, J. J. Fernández-Rossier, *Phys. Rev. B* **2013**, *87*, 075451.
[12] Q. Feng, Y. Zhu, J. Hong, M. Zhang, W. Duan, N. Mao, J. Wu, H. Xu, F. Dong, F. Lin, *Adv. Mater.* **2014**, *26*, 2648.
[13] H. Li, X. Duan, X. Wu, X. Zhuang, H. Zhou, Q. Zhang, X. Zhu, W. Hu, P. Ren, P. Guo, *J. Am. Chem. Soc.* **2014**, *136*, 3756.
[14] M. Geshi, T. Fukazawa, *Phys. B* **2013**, *411*, 154.
[15] F. Ke, Y. Chen, K. Yin, J. Yan, H. Zhang, Z. Liu, S. T. John, J. Wu, H.-K. Mao, B. Chen, *Proc. Natl. Acad. Sci. USA* **2019**, *116*, 9186.
[16] Y. Zhang, M. Heiranian, B. Janicek, Z. Budrikis, S. Zapperi, P. Y. Huang, H. T. Johnson, N. R. Aluru, J. W. Lyding, N. Mason, *Nano Lett.* **2018**, *18*, 2098.
[17] Y. Wang, S. Yao, P. Liao, S. Jin, Q. Wang, M. J. Kim, G. J. Cheng, W. Wu, *Adv. Mater.* **2020**, *32*, 2002342.
[18] K. He, C. Poole, K. F. Mak, J. Shan, *Nano Lett.* **2013**, *13*, 2931.
[19] Y. Chen, Y. Lei, Y. Li, Y. Yu, J. Cai, M.-H. Chiu, R. Rao, Y. Gu, C. Wang, W. Choi, *Nature* **2020**, *577*, 209.
[20] A. von Hippel, *J. Chem. Phys.* **1948**, *16*, 372.
[21] M. Peng, R. Xie, Z. Wang, P. Wang, F. Wang, H. Ge, Y. Wang, F. Zhong, P. Wu, J. Ye, *Sci. Adv.* **2021**, *7*, eabf7358.
[22] M. Amani, C. Tan, G. Zhang, C. Zhao, J. Bullock, X. Song, H. Kim, V. R. Shrestha, Y. Gao, K. B. Crozier, *ACS Nano* **2018**, *12*, 7253.
[23] L. Tong, X. Huang, P. Wang, L. Ye, M. Peng, L. An, Q. Sun, Y. Zhang, G. Yang, Z. Li, *Nat. Commun.* **2020**, *11*, 2308.
[24] L. A. Ba, M. Döring, V. Jamier, C. Jacob, *Org. Biomol. Chem.* **2010**, *8*, 4203.
[25] B. Wu, X. Liu, J. Yin, H. Lee, *Mater. Res. Express* **2017**, *4*, 095902.
[26] X. Huang, J. Guan, Z. Lin, B. Liu, S. Xing, W. Wang, J. Guo, *Nano Lett.* **2017**, *17*, 4619.
[27] A. Kramer, M. L. Van de Put, C. L. Hinkle, W. G. Vandenberghe, *NPJ 2D Mater Appl* **2020**, *4*, 10.
[28] Z. Zhu, X. Cai, C. Niu, C. Wang, Q. Sun, X. Han, Z. Guo, Y. Jia, arXiv preprint **2016**, arXiv:1605.03253.
[29] G. H. Ahn, M. Amani, H. Rasool, D. H. Lien, J. P. Mastandrea, J. W. Ager Iii, M. Dubey, D. C. Chrzan, A. M. Minor, A. Javey, *Nat. Commun.* **2017**, *8*, 608.
[30] G. Plechinger, A. Castellanos-Gomez, M. Buscema, H. S. van der Zant, G. A. Steele, A. Kuc, T. Heine, C. Schueller, T. Korn, *2D Mater.* **2015**, *2*, 015006.
[31] N. Hussain, M.-H. Zhang, Q. Zhang, Z. Zhou, X. Xu, M. Murtaza, R. Zhang, H. Wei, G. Ou, D. Wang, *ACS Nano* **2019**, *13*, 4496.
[32] N. Hussain, T. Liang, Q. Zhang, T. Anwar, Y. Huang, J. Lang, K. Huang, H. Wu, *Small* **2017**, *13*, 1701349.
[33] N. Hussain, Y. Yisen, R. U. R. Sagar, T. Anwar, M. Murtaza, K. Huang, K. Shehzad, H. Wu, Z. Wang, *Nano Energy* **2021**, *83*, 105790.
[34] J. Shim, S.-H. Bae, W. Kong, D. Lee, K. Qiao, D. Nezich, Y. J. Park, R. Zhao, S. Sundaram, X. Li, *Science* **2018**, *362*, 665.
[35] N. Hussain, S. Ahmed, H. U. Tepe, K. Huang, N. Avishan, S. He, M. Rafique, U. Farooq, T. S. Kasirga, A. Bek, *Small* **2022**, 2204302.
[36] N. Hussain, M. Rafique, T. Anwar, M. Murtaza, J. Liu, F. Nosheen, K. Huang, Y. Huang, J. Lang, H. Wu, *2D Mater.* **2019**, *6*, 045006.
[37] Q. Wang, M. Safdar, K. Xu, M. Mirza, Z. Wang, J. He, *ACS Nano* **2014**, *8*, 7497.
[38] Y. Wang, G. Qiu, R. Wang, S. Huang, Q. Wang, Y. Liu, Y. Du, W. A. Goddard, M. J. Kim, X. Xu, P. D. Ye, W. Wu, *Nat. Electron.* **2018**, *1*, 228.
[39] R. M. Martin, G. Lucovsky, K. Helliwell, *Phys. Rev. B* **1976**, *13*, 1383.
[40] Y. Du, J. Maassen, W. Wu, Z. Luo, X. Xu, P. D. Ye, *Nano Lett.* **2016**, *16*, 6701.
[41] Y. Xiang, S. Gao, R.-G. Xu, W. Wu, Y. Leng, *Nano Energy* **2019**, *58*, 202.
[42] X. Le, J. An, G. Zhang, L. Wang, J. Fan, P. Wang, Y. Xie, *BioResources* **2016**, *11*, 10213.
[43] T. Vasileiadis, S. N. Yannopoulos, *J. Appl. Phys.* **2014**, 116.

[44] J. Kopaczek, K. Yumigeta, A. Ibrahim, M. Y. Sayyad, S. Sinha, R. Sailus, P. Hays, S. T. R. Moosavy, S. Susarla, C. Ataca, *Adv. Electron. Mater.* **2023**, *9*, 2201129.
[45] V. Deshpande, R. Pawar, *Physica* **1965**, *31*, 671.
[46] L. Biadala, F. Liu, M. D. Tessier, D. R. Yakovlev, B. Dubertret, M. Bayer, *Nano Lett.* **2014**, *14*, 1134.
[47] D. Choi, K. S. Jeong, *J. Phys. Chem. Lett.* **2019**, *10*, 4303.
[48] O. Del Pozo-Zamudio, S. Schwarz, M. Sich, I. Akimov, M. Bayer, R. Schofield, E. Chekhovich, B. Robinson, N. Kay, O. Kolosov, *2D Mater.* **2015**, *2*, 035010.
[49] S. Tutihasi, G. Roberts, R. Keezer, R. Drews, *Phys. Rev.* **1969**, *177*, 1143.
[50] T. J. Wax, S. Dey, S. Chen, Y. Luo, S. Zou, J. Zhao, *ACS Omega* **2018**, *3*, 14151.
[51] C. Pu, H. Qin, Y. Gao, J. Zhou, P. Wang, X. Peng, *J. Am. Chem. Soc.* **2017**, *139*, 3302.
[52] H. Kim, S. Z. Uddin, N. Higashitarumizu, E. Rabani, A. Javey, *Science* **2021**, *373*, 448.
[53] G. Kresse, J. Hafner, *Phys. Rev. B* **1993**, *47*, 558.
[54] P. Johari, V. B. Shenoy, *ACS Nano* **2012**, *6*, 5449.
[55] S. Bhattacharyya, A. K. Singh, *Phys. Rev. B* **2012**, *86*, 075454.
[56] R. Kurapati, K. Kostarelos, M. Prato, A. Bianco, *Adv. Mater.* **2016**, *28*, 6052.
[57] G. Kresse, J. Furthmüller, *Phys. Rev. B* **1996**, *54*, 11169.
[58] J. P. Perdew, K. Burke, M. Ernzerhof, *Phys. Rev. Lett.* **1996**, *77*, 3865.
[59] J. Heyd, G. E. Scuseria, M. Ernzerhof, *J. Chem. Phys.* **2003**, *118*, 8207.
[60] S. Grimme, *J. Comput. Chem.* **2006**, *27*, 1787.
[61] C. Wang, X. Zhou, J. Qiao, L. Zhou, X. Kong, Y. Pan, Z. Cheng, Y. Chai, W. Ji, *Nanoscale* **2018**, *10*, 22263.
[62] J. Wang, Y. Guo, C. Qiao, H. Shen, R. Zhang, Y. Zheng, L. Chen, S. Wang, Y. Jia, W.-S. Su, *Chinese Journal of Physics* **2019**, *62*, 172.